

Phase-field-based lattice Boltzmann model for liquid-gas-solid flow

Qiang He, Yongjian Li, Weifeng Huang,* Yang Hu, and Yuming Wang
Department of Mechanical Engineering, Tsinghua University, Beijing 10084, China



(Received 5 May 2019; published 24 September 2019)

Based on phase-field theory, we develop a lattice Boltzmann (LB) model for liquid-gas-solid flow from multiphase and particle dynamics algorithms. A modified bounce-back method is developed for the velocity-based LB approach. A curved boundary treatment with second-order accuracy based on velocity interpolation is developed. We propose a predictor-corrector scheme algorithm for specifying the three-phase contact angle on curved boundaries within the framework of structured Cartesian grids. In order to make the algorithm more stable, we combine the implicit particle velocity update scheme and the Galilean invariant momentum exchange method. The proposed method is validated through several single- and multicomponent fluid test cases. It was found the surface tension force associated with the interface acting on the solid structures can be captured. We simulate the sinking of a circular cylinder due to gravity, the numerical results agree well with the experimental data. Finally, we apply the method to the self-assembly process of multiple floating cylinders on water surface.

DOI: [10.1103/PhysRevE.100.033314](https://doi.org/10.1103/PhysRevE.100.033314)

I. INTRODUCTION

Liquid-gas-solid (LGS) systems widely exist in many areas such as electronics fabrication by ink-jet printing [1], emulsion/foam stabilization in foods [2], and cosmetics [3]. However, in these physical situations that involve multiple fluid components and solid particles, it is difficult to investigate experimentally. Alternatively, the numerical simulations can be a powerful tool to obtain useful information, and help to improve the designing procedures.

For LGS flow problems, the challenges mainly arise from the interactions among different phases and the interface tracking. In addition, the influence of arbitrary-shaped geometries and moving boundaries must be taken into consideration for practical simulations. A numerical method for LGS must combine a two-phase flow with a solver for the suspended solid phase. Many LGS simulation approaches [4–6] do not fully resolve the actual particle geometry within the flow. These algorithms simulate the presence of particles by incorporating point forces, associated with particle drag and other forces. This approach fails to capture the detailed interaction between solid objects and fluids when the object size is not negligible. Hence, in many situations, a two-way coupling between the particles and fluids is needed.

As a promising numerical technique in computational fluid dynamics, the lattice Boltzmann method (LBM) has proven to be an efficient method for simulating particle-laden single-phase flows [7–9] and multiphase flows. There are several popular multiphase LBM models, including the color-gradient model [10], the free-energy model [11], and the Shan-Chen (SC) model [12]. A few groups combined multiphase lattice Boltzmann solvers with the known algorithms for suspended particles to simulate LGS and fluid-fluid-solid (FFS) flow. We use FFS instead of LGS to distinguish between systems with

less difference in fluid properties. According to the multiphase models, the existing schemes mainly fall into two categories, including the phase-field-based model [13–15] and the SC model [16–18]. Stratford *et al.* [13–15] used a combination of the LBM phase-field-based model and particle dynamics to simulate a FFS flow, and their simulations shown formation of a class of gels, continuous interfacially jammed emulsion gel (bijels), which was experimentally confirmed later [19]. Another group [20] developed a similar LBM algorithm using a phase-field-based model to handle the multiple fluid components with high-density ratio, and then they investigated the influence of particles on the dynamics and eventual rupture of stretching liquid bridges in a drop-forming case [20]. However, more work is focused on the SC method. Onishi *et al.* [21] combined a SC multicomponent model and a particle dynamics algorithm to simulate capillary interactions between colloidal particles at fluid-fluid interfaces. Since then, many scholars proposed similar models based on the SC method for LGS/FFS flow. Joshi *et al.* [16] investigated wetting dynamics and particle deposition for an evaporating colloidal drop in three dimensions. Jansen *et al.* [22] studied the transition from bijels to Pickering emulsions and found the transition was dependent on the contact angle, the particle concentration, and the ratio of the solvents. Günther *et al.* [18] investigated the anisotropic particles at liquid interfaces and found the ellipsoidal particles could lead to a transition between bijels and Pickering emulsions. Davies *et al.* [23] studied the detachment energies of spheroidal particles from liquid-liquid interfaces. Chen *et al.* [24] proposed a modified wetting model to reduce the nonphysical effects to simulate FFS flow. Lang *et al.* [25] studied the self-assemblies of colloidal particles on the substrate due to the capillary forces.

In the existing schemes, the multicomponent algorithm is handled differently, either with the SC model or a different phase-field-based model, mostly. The SC method is easier to implement, as the interface forms naturally due to interactions between different fluid components. The phase-field method

*Corresponding author: huangwf@mail.tsinghua.edu.cn

is based on a phase-field equation such as four-order Cahn-Hilliard equation, which can be solved to track the interface using LBM. The algorithm of these SC models cannot resolve that the liquid-gas interface with a high-density difference and the density ratio is on the order of $O(10)$, which is much smaller than the density ratio of most liquid-gas two-phase flows. The LGS model proposed by Connington *et al.* [20] reaches high-density ratios for special cases, but the algorithm based on the Cahn-Hilliard equation is very complicated and a supplemental force must be added to recover the appropriate physics when a particle is immersed in the fluid-fluid interface in their model. In this paper, we develop a LBM model for LGS flow based on the conservative Allen-Cahn phase-field theory, which only contains a second-order gradient term, and therefore, the present model can achieve a higher numerical accuracy in interface tracking than the previous model based on the fourth-order Cahn-Hilliard equation. We mainly use the multiphase algorithm developed by Fakhari *et al.* [26], in which a modified velocity distribution function is used. A modified bounce-back scheme is developed based on the velocity distribution function. We also propose an algorithm for prescribing the three-phase contact angle on curved boundaries without using a staircase approximation for the solid boundary.

This paper is organized as follows. In Sec. II, after a description of the phase-field approach for multiphase lattice Boltzmann simulations and an extension of the lattice Boltzmann method to simulate suspensions, a way to combine the two methods is proposed. In Sec. III, we first demonstrate that the method is accurate when solid objects are contained inside bulk fluid regions of the flow, then the contact line motion on a single circular cylinder is studied. Moreover, the suitability of the new method is tested by performing studies of sinking dynamics of a circular cylinder from the water surface due to gravity and the self-assembly process of multiple floating cylinders on the water surface.

II. NUMERICAL MODELING

A. Multiphase lattice Boltzmann model

The interface-tracking equation in this study is built upon the conservative Allen-Cahn equation, in this model, the phase-field ϕ assumes two extreme values, $\phi_L = 0$ and $\phi_H = 1$, in the bulk of the light and heavy fluids, respectively. The phase-field equation governs the evolution of the interface between the two fluids [27]

$$\frac{\partial \phi}{\partial t} + \nabla \cdot (\mathbf{u}\phi) = \nabla \cdot M_\phi \left[\left(\nabla \phi - \frac{4\phi(1-\phi)\hat{\mathbf{n}}}{\xi} \right) \right], \quad (1)$$

where M_ϕ and ξ are the mobility efficient and the interfacial width, respectively, and $\hat{\mathbf{n}}$ is the unit vector out of normal to the interface:

$$\hat{\mathbf{n}} = \frac{\nabla \phi}{|\nabla \phi|}. \quad (2)$$

For an interface located at \mathbf{x}_0 and at thermodynamic equilibrium, the phase-field distribution at \mathbf{x} assumes a hyperbolic

tangent profile:

$$\phi(\mathbf{x}) = \frac{1}{2} \left[1 \pm \tanh \left(\frac{2|\mathbf{x}-\mathbf{x}_0|}{\xi} \right) \right]. \quad (3)$$

The corresponding multiple-relaxation-time (MRT) LB equation for phase-field parameter ϕ can be expressed as

$$\begin{aligned} h_i(\mathbf{x} + \mathbf{e}_i \delta_t, t + \delta_t) - h_i(\mathbf{x}, t) \\ = (\mathbf{M}^{-1} \mathbf{S}^h \mathbf{M})_{ij} [h_j(\mathbf{x}, t) - h_j^{\text{eq}}(\mathbf{x}, t)] \\ + \left[\mathbf{M}^{-1} \left(\mathbf{I} - \frac{\mathbf{S}^h}{2} \right) \mathbf{M} \right]_{ij} G_j \delta_t, \end{aligned} \quad (4)$$

in which the forcing term is given by

$$G_j = w_j \frac{4}{\xi} \phi (1 - \phi) \mathbf{e}_j \cdot \hat{\mathbf{n}}. \quad (5)$$

The D2Q9 velocity model (two dimensions with nine lattice velocities) is employed here, where the velocity set is given as

$$\mathbf{e}_i = \begin{cases} (0, 0), & i = 0, \\ (\cos[(i-1)\frac{\pi}{2}], \sin[(i-1)\frac{\pi}{2}])c, & i = 1 \sim 4, \\ (\cos[(2i-1)\frac{\pi}{2}], \sin[(2i-1)\frac{\pi}{2}])c, & i = 5 \sim 8, \end{cases} \quad (6)$$

where $c = \delta_x / \delta_t = 1$ and δ_x and δ_t are the lattice length scale and time scale, the corresponding weight coefficients are given as

$$\mathbf{e}_i = \begin{cases} \frac{4}{9} & i = 0, \\ \frac{1}{9}, & i = 1 \sim 4, \\ \frac{1}{36} & i = 5 \sim 8. \end{cases} \quad (7)$$

The equilibrium phase-field distribution function is

$$h_i^{\text{eq}} = w_i \phi \left(1 + \frac{\mathbf{e}_i \cdot \mathbf{u}}{c_s^2} + \frac{(\mathbf{e}_i \cdot \mathbf{u})^2}{2c_s^4} - \frac{|\mathbf{u}|^2}{2c_s^2} \right), \quad (8)$$

where c_s is the lattice sound speed and usually set to be $c/\sqrt{3}$ for isothermal flows.

In the MRT collision model, \mathbf{M} is the transformation matrix, which is defined as

$$\mathbf{M} = \begin{pmatrix} 1 & 1 & 1 & 1 & 1 & 1 & 1 & 1 & 1 \\ -4 & -1 & -1 & -1 & -1 & 2 & 2 & 2 & 2 \\ 4 & -2 & -2 & -2 & -2 & 1 & 1 & 1 & 1 \\ 0 & 1 & 0 & -1 & 0 & 1 & -1 & -1 & 1 \\ 0 & -2 & 0 & 2 & 0 & 1 & -1 & -1 & 1 \\ 0 & 0 & 1 & 0 & -1 & 1 & -1 & -1 & -1 \\ 0 & 0 & -2 & 0 & 2 & 1 & 1 & -1 & -1 \\ 0 & 1 & -1 & 1 & -1 & 0 & 1 & 0 & 0 \\ 0 & 0 & 0 & 0 & 0 & 1 & -1 & 1 & -1 \end{pmatrix}, \quad (9)$$

\mathbf{S}^h is the diagonal matrix, which can be written as

$$\mathbf{S}^h = \text{diag}(s_0^h, s_1^h, s_2^h, s_3^h, s_4^h, s_5^h, s_6^h, s_7^h, s_8^h), \quad (10)$$

and $s_3^h = s_5^h = \frac{1}{\tau_\phi}$, where τ_ϕ is determined by the mobility coefficient M_ϕ ,

$$M_\phi = c_s^2 \left(\tau_\phi - \frac{1}{2} \right) \delta t. \quad (11)$$

The other s_i^h are chosen as $s_0^h = 1.0$, $s_1^h = s_2^h = 1.1$, $s_4^h = s_6^h = s_3^h = s_5^h$, $s_7^h = s_8^h = 1.2$.

The phase-field value is then calculated by taking the zeroth moment of the phase-field distribution function

$$\phi = \sum_i h_i. \quad (12)$$

The continuity and momentum equations for incompressible multiphase flows are given by

$$\nabla \cdot \mathbf{u} = 0, \quad (13)$$

$$\rho \left(\frac{\partial \mathbf{u}}{\partial t} + \nabla \cdot (\mathbf{u}\mathbf{u}) \right) = -\nabla p + \nabla \cdot [\mu(\nabla \mathbf{u} + (\nabla \mathbf{u})^T)] + \mathbf{F}_s + \mathbf{F}_b, \quad (14)$$

where ρ and μ are the density and dynamic viscosity of the fluid, respectively, p is the hydrodynamic pressure, \mathbf{F}_b is the body force, \mathbf{F}_s is the surface tension, which can be calculated by $\mathbf{F}_s = \mu_\phi \nabla \phi$, and μ_ϕ is the chemical potential

$$\mu_\phi = 4\beta\phi(\phi - 1)(\phi - 0.5) - \kappa \nabla^2 \phi. \quad (15)$$

The coefficients β and κ are related to the surface tension σ and interface thickness ξ by

$$\beta = \frac{12\sigma}{\xi}, \quad \kappa = \frac{3\sigma\xi}{2}. \quad (16)$$

Following the work of Zu and He [28], Eq. (14) can be rewritten as the following velocity-based hydrodynamics equation:

$$\frac{\partial \mathbf{u}}{\partial t} + \nabla \cdot (\mathbf{u}\mathbf{u}) = -\nabla \left(\frac{p}{\rho} \right) + \nabla \cdot [v(\nabla \mathbf{u} + (\nabla \mathbf{u})^T)] + \frac{\mathbf{F}_{\text{total}}}{\rho}, \quad (17)$$

where $v = \mu/\rho$ is the kinematic viscosity and $\mathbf{F}_{\text{total}}$ is defined as

$$\mathbf{F}_{\text{total}} = \mathbf{F}_s + \mathbf{F}_b + \mathbf{F}_v + \mathbf{F}_p, \quad (18)$$

$$\mathbf{F}_v = v(\nabla \mathbf{u} + (\nabla \mathbf{u})^T) \cdot \nabla \rho, \quad (19)$$

$$\mathbf{F}_p = -\frac{p}{\rho} \nabla \rho. \quad (20)$$

The MRT model with an external force term will be adopted instead of the lattice Boltzmann BGK models (LBGK) to avoid the unphysical, numerical artifact and improve the stability, which is written as [29]

$$\begin{aligned} & f_i(\mathbf{x} + \mathbf{e}_i \delta t, t + \delta t) - f_i(\mathbf{x}, t) \\ &= (\mathbf{M}^{-1} \mathbf{S}^f \mathbf{M})_{ij} [f_j(\mathbf{x}, t) - f_j^{\text{eq}}(\mathbf{x}, t)] \\ &+ \left[\mathbf{M}^{-1} \left(\mathbf{I} - \frac{\mathbf{S}^f}{2} \right) \mathbf{M} \right]_{ij} \mathbf{F}_j \delta t \end{aligned} \quad (21)$$

with \mathbf{M} a 9×9 transform matrix and \mathbf{S}^f a relaxation matrix, $f_i^{\text{eq}}(\mathbf{x}, t)$ is the modified equilibrium distribution function for incompressible fluids given by

$$f_i^{\text{eq}} = w_i \left(\frac{p}{\rho c_s^2} + \frac{\mathbf{e}_i \cdot \mathbf{u}}{c_s^2} + \frac{(\mathbf{e}_i \cdot \mathbf{u})^2}{2c_s^4} - \frac{|\mathbf{u}|^2}{2c_s^2} \right). \quad (22)$$

\mathbf{S}^f is the diagonal matrix, which can be written as

$$\mathbf{S}^f = \text{diag}(s_0^f, s_1^f, s_2^f, s_3^f, s_4^f, s_5^f, s_6^f, s_7^f, s_8^f), \quad (23)$$

where

$$s_7^f = s_8^f = \frac{1}{\tau_s + 0.5}, \quad (24)$$

and τ_s is the hydrodynamic relaxation time, which is related to the viscosity and density of fluid by

$$\tau_s = \frac{\mu}{\rho c_s^2 \delta t}. \quad (25)$$

The other s_i^f are set as follows: $s_0^f = s_3^f = s_5^f = 0$ for the conserved moments, $s_1^f = 1.64$, $s_2^f = 1.54$, $s_4^f = s_6^f = 1.9$, and τ_L and τ_H are the relaxation rates for the light and heavy fluids, respectively.

To calculate the relaxation time from the phase field, the dynamics viscosity μ and the density ρ can be calculated by a simple linear interpolation [26]

$$\mu = \mu_L + \phi(\mu_H - \mu_L), \quad (26)$$

$$\rho = \rho_L + \phi(\rho_H - \rho_L), \quad (27)$$

where μ_L and μ_H are the viscosities ρ_L and ρ_H are the bulk densities of the light phase and heavy phase.

The force term \mathbf{F}_j is obtained using the Guo-Zheng-Shi model [30]:

$$\mathbf{F}_j = w_j \left(\frac{\mathbf{e}_i - \mathbf{u}}{c_s^2} + \frac{\mathbf{e}_i \cdot \mathbf{u}}{c_s^2} \mathbf{e}_i \right) \cdot \frac{\mathbf{F}_{\text{total}}}{\rho}. \quad (28)$$

Through the Chapman-Enskog expansion, the pressure p and velocity \mathbf{u} can be derived, respectively, as the zeroth and first order moments of f_i ,

$$p = \rho c_s^2 \sum_i f_i, \quad (29)$$

$$\mathbf{u} = \sum_i \mathbf{e}_i f_i + \frac{1}{2} \frac{\mathbf{F}_{\text{total}}}{\rho} \delta t. \quad (30)$$

One of the advantages of the LBM is that the deviatoric stress tensor can be locally obtained in terms of the hydrodynamic distribution function:

$$\begin{aligned} & v[\nabla \mathbf{u} + (\nabla \mathbf{u})^T] \\ &= -\frac{v}{c_s^2 \delta t} \left[\sum_i \mathbf{e}_i \mathbf{e}_i \sum_j (\mathbf{M}^{-1} \mathbf{S}^f \mathbf{M})_{ij} (f_j - f_j^{\text{eq}}) \right]. \end{aligned} \quad (31)$$

Additionally, we compute the gradient of the phase-field using second-order isotropic centered differences

$$\nabla \phi = \frac{c}{c_s^2 \delta t} \sum_i \mathbf{e}_i w_i \phi(\mathbf{x} + \mathbf{e}_i \delta t, t), \quad (32)$$

and its Laplacian is calculated by

$$\nabla^2 \phi = \frac{2c^2}{c_s^2 \delta t} \sum_i w_i [\phi(\mathbf{x} + \mathbf{e}_i \delta t, t) - \phi(\mathbf{x}, t)]. \quad (33)$$

B. Particle dynamics

In order to apply the LB approach to simulate the LGS flows, two issues should be carefully considered. One is how to treat the boundary conditions on a particle surface, and the other is how to calculate the hydrodynamic forces exerted on the solid particle.

In this study, the velocity-based LB approach proposed by Zu and He [28] is applied. A boundary link is defined as joining a fluid node at \mathbf{x}_b , denoted as the boundary node, to one solid node inside the particle at $\mathbf{x}_b + \mathbf{e}_b \delta t$. When a momentum exchange scheme is applied, the distribution function changes its ‘‘momentum’’ from $\rho f_b \mathbf{e}_b$ to $\rho f_b^u \mathbf{e}_b$, where the unknown distribution function f_b^u of the boundary node can be calculated by the curved boundary scheme described below and the boundary link $\mathbf{e}_b = -\mathbf{e}_b$. Therefore, the change in momentum of the distribution is $\Delta M = \rho f_b^u \mathbf{e}_b - \rho f_b \mathbf{e}_b = \rho(f_b^u - f_b) \mathbf{e}_b$. Then an equal and opposite change in momentum must be applied to the macroscopic solid particle. Hence, an impulse of force and corresponding torque is applied to the solid particle:

$$\mathbf{F}(\mathbf{e}_b; \mathbf{x}_b) = \rho_{\mathbf{x}_b} (f_b^u - f_b) \mathbf{e}_b, \quad (34)$$

$$\mathbf{T}(\mathbf{e}_b; \mathbf{x}_b) = (\mathbf{x}_w - \mathbf{X}) \times \rho_{\mathbf{x}_b} (f_b^u - f_b) \mathbf{e}_b, \quad (35)$$

where \mathbf{x}_w is the wall position on the fluid-solid link, and \mathbf{X} is the center of mass of the solid particle. For the case of moving walls, the total force and torque on a particle is computed by taking the summation of all impulses that were computed:

$$\mathbf{F}_p = \frac{\delta x^2}{\delta t} \sum_{\mathbf{x}_b} \rho_{\mathbf{x}_b} [(\mathbf{e}_b - \mathbf{u}_w(t)) f_b - (\mathbf{e}_b - \mathbf{u}_w(t)) f_b^u], \quad (36)$$

$$\begin{aligned} \mathbf{T}_p &= \frac{\delta x^2}{\delta t} \sum_{\mathbf{x}_b} \rho_{\mathbf{x}_b} (\mathbf{x}_w - \mathbf{X}) \\ &\times [(\mathbf{e}_b - \mathbf{u}_w(t)) f_b - (\mathbf{e}_b - \mathbf{u}_w(t)) f_b^u], \end{aligned} \quad (37)$$

where $\mathbf{u}_w(t) = \mathbf{U}(t) + \boldsymbol{\Omega}(t) \times (\mathbf{x}_w - \mathbf{X})$, $\mathbf{U}(t)$ is the particle velocity, and $\boldsymbol{\Omega}(t)$ is the angular velocity. Note that a modified momentum exchange (ME) scheme is adopted here for the fulfillment of the Galilean invariance [31].

An implicit update method [32] combined with the modified ME [31] is used to update the particle velocity and angular velocity. Applying the bounce-back algorithm for moving walls, the f_b^u and h_b^u can be written as [33]

$$f_b^u = f_b - \frac{2w_b \mathbf{u}_w(t + \delta t) \cdot \mathbf{e}_b}{c_s^2}, \quad (38)$$

$$h_b^u = -h_b + 2\phi w_i. \quad (39)$$

Hence, neglecting the terms $O(\mathbf{u}_w^2)$, the total force and torque on a colloid can be split into a velocity-dependent and a velocity-independent part and the governing equations of motion for particles are given as

$$\begin{aligned} \begin{pmatrix} m_0 \mathbf{U}(t + \delta t) \\ I_0 \boldsymbol{\Omega}(t + \delta t) \end{pmatrix} &= \begin{pmatrix} m_0 \mathbf{U}(t) \\ I_0 \boldsymbol{\Omega}(t) \end{pmatrix} + \delta t \left[\begin{pmatrix} \mathbf{F}_0 \\ \mathbf{T}_0 \end{pmatrix} \right. \\ &\left. - \begin{pmatrix} \psi^{\text{FU}} & \psi^{\text{F}\Omega} \\ \psi^{\text{TU}} & \psi^{\text{T}\Omega} \end{pmatrix} \begin{pmatrix} \mathbf{U}(t + \delta t) \\ \mathbf{T}(t + \delta t) \end{pmatrix} \right], \end{aligned} \quad (40)$$

where the matrices ψ are interpreted as drag coefficients, the velocity independent parts of the force \mathbf{F}_0 and the torque \mathbf{T}_0 are

$$\mathbf{F}_0 \left(t + \frac{1}{2} \delta t \right) = \frac{\delta x^2}{\delta t} \sum_{\mathbf{x}_b} \rho_{\mathbf{x}_b} [(f_b + f_b) \mathbf{e}_b - (f_b - f_b) \mathbf{u}_w(t)], \quad (41)$$

$$\begin{aligned} \mathbf{T}_0 \left(t + \frac{1}{2} \delta t \right) &= \frac{\delta x^2}{\delta t} \sum_{\mathbf{x}_b} \rho_{\mathbf{x}_b} [(f_b + f_b) (\mathbf{x}_w - \mathbf{X}) \\ &\times \mathbf{e}_i + (f_b - f_b) (\mathbf{x}_w - \mathbf{X}) \times \mathbf{u}_w(t)], \end{aligned} \quad (42)$$

where the sum is over all the boundary nodes b describes the particle surface. It is noted that f_b is equal to f_b when applying the halfway bounce-back scheme.

Considering the situation when two particles are close to contact some of the boundary nodes are missing and the surfaces are no longer closed, the matrices ψ can be written as

$$\begin{aligned} \psi^{\text{FU}} &= \frac{2\delta x^3}{c_s^2 \delta t} \sum_{\mathbf{x}_b} \rho_{\mathbf{x}_b} w_b (\mathbf{e}_b + \mathbf{u}_w(t)) (\mathbf{e}_b - \bar{\mathbf{e}}_b), \\ \psi^{\text{F}\Omega} &= \frac{2\delta x^3}{c_s^2 \delta t} \sum_{\mathbf{x}_b} \rho_{\mathbf{x}_b} w_b (\mathbf{e}_b + \mathbf{u}_w(t)) (\mathbf{r}_b \times \mathbf{e}_b - \overline{\mathbf{r}_b \times \mathbf{e}_b}), \\ \psi^{\text{T}\Omega} &= \frac{2\delta x^3}{c_s^2 \delta t} \sum_{\mathbf{x}_b} \rho_{\mathbf{x}_b} w_b [\mathbf{r}_b \times (\mathbf{e}_b + \mathbf{u}_w(t))] [\mathbf{e}_b - \bar{\mathbf{e}}_b], \\ \psi^{\text{T}\Omega} &= \frac{2\delta x^3}{c_s^2 \delta t} \sum_{\mathbf{x}_b} \rho_{\mathbf{x}_b} w_b [\mathbf{r}_b \times (\mathbf{e}_b + \mathbf{u}_w(t))] [\mathbf{r}_b \times \mathbf{e}_b - \overline{\mathbf{r}_b \times \mathbf{e}_b}], \end{aligned} \quad (43)$$

where $\bar{\mathbf{e}}_b = \frac{\sum_{\mathbf{x}_b} w_b \mathbf{e}_b}{\sum_{\mathbf{x}_b} w_b}$, $\overline{\mathbf{r}_b \times \mathbf{e}_b} = \frac{\sum_{\mathbf{x}_b} w_b \mathbf{r}_b \times \mathbf{e}_b}{\sum_{\mathbf{x}_b} w_b}$.

C. Curved boundary treatment

The curved boundary condition should be implemented for a body with complex geometry that is frequently encountered in the simulation of particulate flows. The main concern is to determine the unknown distribution function of the boundary node, and for that, we decompose the distribution of fictitious node into two parts, i.e., the nonequilibrium part and the equilibrium part. The nonequilibrium part is obtained from the bounce-back rule. In order to obtain the equilibrium part, we interpolate the velocity firstly, and then calculate the equilibrium function using Eqs. (8) and (22).

The idea is to construct the population of the fictitious node at location \mathbf{x}_F that will travel to \mathbf{x}_f after bouncing back on the wall \mathbf{x}_w . We use different neighboring distributions to interpolate velocity, and, as illustrated in Fig. 1, the interpolation expressions are

$$\mathbf{u}(\mathbf{x}_F, t) = \begin{cases} 2q\mathbf{u}(\mathbf{x}_f, t) + (1 - 2q)\mathbf{u}(\mathbf{x}_{f_f}, t), & 0 \leq q < 1/2 \\ \frac{1-q}{q}\mathbf{u}(\mathbf{x}_f, t) + \frac{2q-1}{q}\mathbf{u}(\mathbf{x}_w, t), & 1/2 \leq q < 1 \end{cases} \quad (44)$$

where the parameter $q = |\mathbf{x}_f - \mathbf{x}_w| / |\mathbf{x}_f - \mathbf{x}_b|$.

In order to calculate the $h_b^{\text{eq}}(\mathbf{x}_f, t + \Delta t)$ and $f_b^{\text{eq}}(\mathbf{x}_f, t + \Delta t)$, the phase field $\phi(\mathbf{x}_F, t)$ and pressure $p(\mathbf{x}_F, t)$ are needed. The pressure $p(\mathbf{x}_F, t)$ could be approximated by the pressure of boundary node $p(\mathbf{x}_f, t)$, because dimensional analysis shows that $\partial_\alpha p \sim O(Ma^2)$ [34]. The phase field

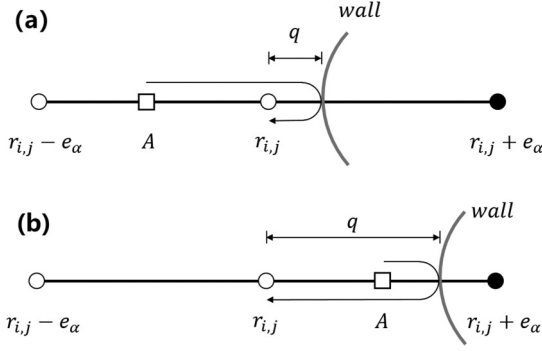


FIG. 1. Schematic diagrams of the velocity interpolation rules: (a) $0 \leq q < 1/2$, (b) $1/2 \leq q < 1$.

$\phi(\mathbf{x}_F, t)$ is calculated by

$$\phi(\mathbf{x}_F, t) = 2q\phi(\mathbf{x}_f, t) + (1 - 2q)\phi(\mathbf{x}_{ff}, t), \quad (45)$$

but when $1/2 \leq q < 1$, Eq. (45) turns out to be an extrapolation method, and to obtain a reasonable phase-field value, a correction scheme is adopted:

$$\phi(\mathbf{x}_F, t) = \begin{cases} \phi_L, & \phi(\mathbf{x}_F, t) < \phi_L \\ \phi_H, & \phi(\mathbf{x}_F, t) > \phi_H \end{cases}. \quad (46)$$

Based on the velocity obtained, and the pressure and phase-field value, we can calculate the equilibrium distribution of the fictitious node that will travel to \mathbf{x}_f . The nonequilibrium distribution is obtained from the bounce-back rule

$$h_b^{\text{neq}}(\mathbf{x}_f, t + \Delta t) = -h_b^{\text{neq}}(\mathbf{x}_f, t), \quad (47)$$

$$f_b^{\text{neq}}(\mathbf{x}_f, t + \Delta t) = f_b^{\text{neq}}(\mathbf{x}_f, t). \quad (48)$$

To impose a specified contact angel at a solid boundary, the following condition has been proposed [35]:

$$\mathbf{n}_w \cdot \nabla \phi|_{\mathbf{x}_w} = \Theta \phi_w (1 - \phi_w), \quad \Theta = -\sqrt{\frac{2\beta}{k}} \cos \theta, \quad (49)$$

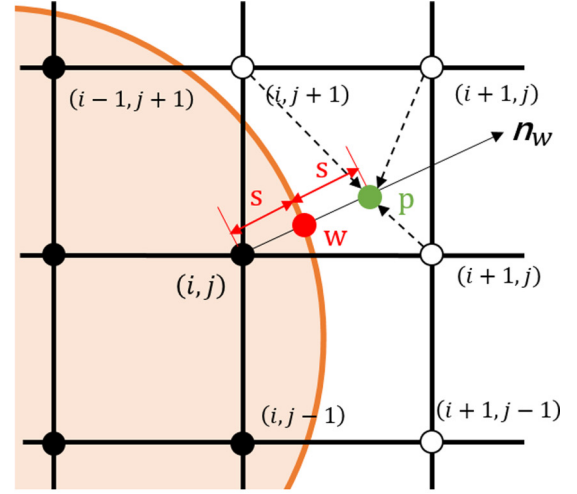
where ϕ_w is the phase-field value at the wall, \mathbf{n}_w is the unit vector normal to the solid wall. In order to apply the wetting condition on a curved boundary, we need the unit vector normal to the solid wall (\mathbf{n}_w) along with the gradient of the phase field $\nabla \phi|_{\mathbf{x}_w}$ and its value ϕ_w . To this end we build a predictor-corrector scheme by modifying the method proposed by Fakhari [36].

A schematic implementation of this method for a typical boundary node is illustrated in Fig. 2(a). In order to obtain the unknown phase-field value at the boundary node $\phi_{i,j}$, we use a centered difference for the left-hand-side of Eq. (49) to obtain

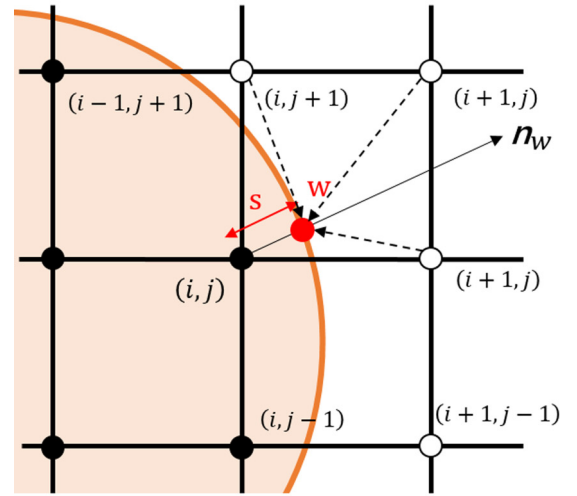
$$\mathbf{n}_w \cdot \nabla \phi|_{\mathbf{x}_w} = \frac{\partial \phi}{\partial \mathbf{n}_w} \Big|_{\mathbf{x}_w} = \frac{\phi_p - \phi_{i,j}}{2s} = \Theta \phi_w (1 - \phi_w), \quad (50)$$

where $s = |\mathbf{x}_w - \mathbf{x}_{i,j}|$ is the distance between the solid wall and the interpolated point, which is known given the location of the wall boundary.

We eliminate ϕ_w in Eq. (50) by using $\phi_w = (\phi_p + \phi_{i,j})/2$. Then a quadratic equation is obtained, the solution of which



(a)



(b)

FIG. 2. Schematic depicting the interpolation to obtain the unknown phase-field value $\phi_{i,j}$ of two schemes. (a) the common method, (b) the alternative scheme when the common method fails.

gives

$$\phi_{i,j} = \frac{1}{\varsigma} (1 + \varsigma - \sqrt{(1 + \varsigma)^2 - 4\varsigma\phi_p}) - \phi_p, \quad (51)$$

$$\varsigma = s\Theta \neq 0 \quad (\theta \neq 90^\circ).$$

For neutral wetting conditions ($\theta = 90^\circ$), the solution would be $\phi_{i,j} = \phi_p$. As for now, our approach shares the same ideas with the method of Fakhari [36]. Then the last question is how to calculate the only unknown quantity ϕ_p . Fakhari [36] used a bidirectional interpolation to find ϕ_p , but different interpolation schemes are needed when the point p locates in different places in the grids. So this approach is difficult to implement and hard to be extended to three-dimensional problems. In this study, we propose a scheme to estimate ϕ_p as follows:

(1) Determine the solid nodes next to a fluid node, which links across the wall. Take the solid node (i, j) in Fig. 2(a) as an example, first calculate the vector \mathbf{s} to find the position of point p :

$$\mathbf{s} = \mathbf{n}_w(R - |\mathbf{r}_{(i,j)} - \mathbf{r}_c|), \mathbf{n}_w = \frac{\mathbf{r}_{(i,j)} - \mathbf{r}_c}{|\mathbf{r}_{(i,j)} - \mathbf{r}_c|}, \quad (52)$$

where \mathbf{r}_c is the center coordinate of the particle, R is the particle radius, then find the fluid node with the minimum distance between the point p , $\min(|\mathbf{r}_{(i,j)} - \mathbf{r}_{\text{adjacent}} + 2\mathbf{s}|)$, and the nearest fluid node in this example is the node $(i + 1, j)$.

(2) Estimate $\nabla\phi_{i+1,j}$ using finite differences using the adjacent seven fluid nodes [excluding two solid nodes (i, j) and $(i, j - 1)$]:

$$\nabla\phi_{i+1,j} = \frac{\sum_{\alpha} \mathbf{e}_{\alpha}(\phi(\mathbf{x} + \mathbf{e}_{\alpha}\delta t, t) - \phi(\mathbf{x}, t))}{\sum_{\alpha} \mathbf{e}_{\alpha} \cdot \mathbf{e}_{\alpha}}. \quad (53)$$

(3) Extrapolate along the links and calculate ϕ_p ,

$$\phi_p = \phi_{i+1,j} + (\mathbf{r}_{i,j} - \mathbf{r}_{i+1,j} + 2\mathbf{s}) \cdot \nabla\phi_{i+1,j}. \quad (54)$$

However, this method fails when the $(1 + \zeta)^2 - 4\zeta\phi_p$ in Eq. (51) is below zero, which may happen with extremely low probability from our experiences. In order to fix this issue, we propose an alternative approach as a substitution as illustrated in Fig. 2(b). We use another difference for the left-hand-side of Eq. (49) to obtain

$$\mathbf{n}_w \cdot \nabla\phi|_{\mathbf{x}_w} = \frac{\partial\phi}{\partial\mathbf{n}_w}|_{\mathbf{x}_w} = \frac{\phi_w - \phi_{i,j}}{s} = \Theta\phi_w(1 - \phi_w), \quad (55)$$

$$K = \frac{1}{\ln W^* - 0.9157 + 1.7244(W^*)^2 - 1.7302(W^*)^{-4} + 2.4056(W^*)^{-6} - 4.5913(W^*)^{-8}}, \quad (58)$$

where $W^* = W/D$. With this analytical solution, we can evaluate the accuracy of the model.

For comparison, the computational parameters in the present simulation are taken to be the same as those used in Ref. [37]. As shown in Fig. 3, the computational domain is $W \times H = 1.2 \text{ cm} \times 6 \text{ cm}$, the diameter of the particle is $D = 0.24 \text{ cm}$, the density and viscosity of the fluid are set to be $\rho_f = 1.0 \text{ g/cm}^3$ and $\mu = 0.1 \text{ g/(cms)}$, respectively. A lattice with size of 120×600 is used to cover the computation domain, and the relaxation time τ_s related to the shear viscosity is set to be 0.3. Initially, the particle is located at the center line (0.6 cm, 3.0 cm) and held at rest (same as the fluid), and the gravity accelerating velocity is $g = 980.0 \text{ cm/s}^2$. In our simulations, zero velocities are applied uniformly at the inflow boundary that is always $12.5 D$ from the moving particle, and the normal derivative of velocity is set to be zero at the outflow boundary, which is $12.5 D$ from the particle.

A number of tests with different particle density ρ_p and Reynolds numbers Re are carried out. Here the particle Reynolds number is defined by $Re = \rho_f U_d D / \mu$, where U_d

is the speed of the terminal settling velocity of the particle.

$$\phi_{i,j} = \phi_w - s\Theta\phi_w(1 - \phi_w). \quad (56)$$

In order to obtain the phase-field value ϕ_w , a similar scheme is applied as described above.

III. RESULTS AND DISCUSSION

The equations were implemented in their nondimensional form using the Reynolds number $Re = \rho_H U D / \mu_H$, the Weber number $We = \rho_H U^2 L / \sigma$, and the Bond number $Bo = \rho_H g L^2 / \sigma$, and $\rho^* = \rho_H / \rho_L$, $\mu^* = \mu_H / \mu_L$ are the density and viscosity ratios of the gas to the liquid, respectively. To obtain numerically stable and reasonably accurate results, the mobility coefficient and interface thickness are fixed as $M_{\phi} = 0.01$ and $\xi = 5$, respectively.

A. Single particle inside bulk

To validate the present method in particulate flows, a circular particle settling in a vertical channel is simulated. At low Reynolds numbers, the terminal sedimentation velocity of the particle can be approximated as [37]

$$\mathbf{U}_d = \frac{D^2}{16K\mu}(\rho_f - \rho_p)\mathbf{g} \quad (57)$$

where μ is the dynamic viscosity of the fluid, \mathbf{g} is the gravitational acceleration, ρ_p and ρ_f are the particle density and fluid density, respectively, and K is a wall correction factor that reflects the effect of the channel walls on the drag force

is the speed of the terminal settling velocity of the particle. In Fig. 1 the velocities from the present model are shown together with the analytical and the simulation results in Ref. [37]. Figure 4 also shows that the results deviate from the analytical solutions given by Eq. (57) as they become larger. This may be because the analytical solution is valid only for small Reynolds numbers.

B. Contact line motion on a stationary circular cylinder

The contact line motion on a single circular cylinder is used here to validate the capability of our model for simulating complicated wetting phenomena. A stationary cylinder with a dimensionless radius of 40 is fixed at the center of a fluid domain and the size of the domain is 240×240 . Wall conditions are applied at all the boundaries. Initially, the lower half part of the domain is occupied by fluid, while gas occupies the rest of the space. We consider two different contact angles, $\theta = 60^\circ$ and $\theta = 120^\circ$ with surface tension $\sigma = 4 \times 10^{-4}$. In this simulation, three cases with different density ratios and viscosity ratios are considered. In these cases, the relaxation

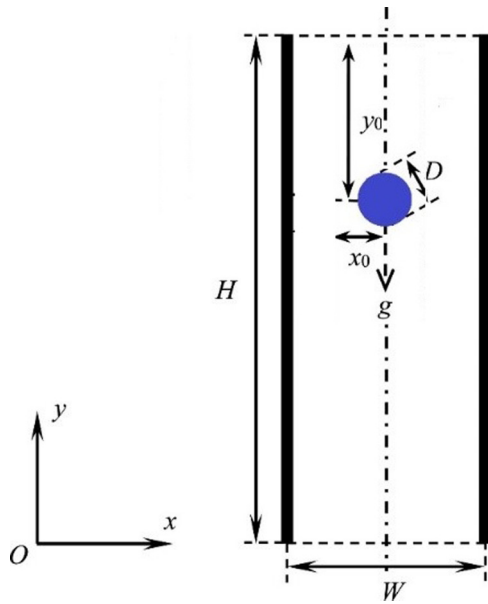


FIG. 3. The schematic diagram for a circular particle settling under gravity in an infinite channel.

time of gas τ_L is set to be 0.3 and τ_H is calculated based on the ρ^* and μ^* :

- Case 1: ($\rho^* = 10, \mu^* = 1$),
- Case 2: ($\rho^* = 100, \mu^* = 10$),
- Case 3: ($\rho^* = 1000, \mu^* = 100$).

Simulation results indicate that the density and viscosity ratios have no effect on the equilibrium profile. Figure 5 shows the contact angles of the stationary cylinder under these two wetting conditions, which agree well with the predicted results.

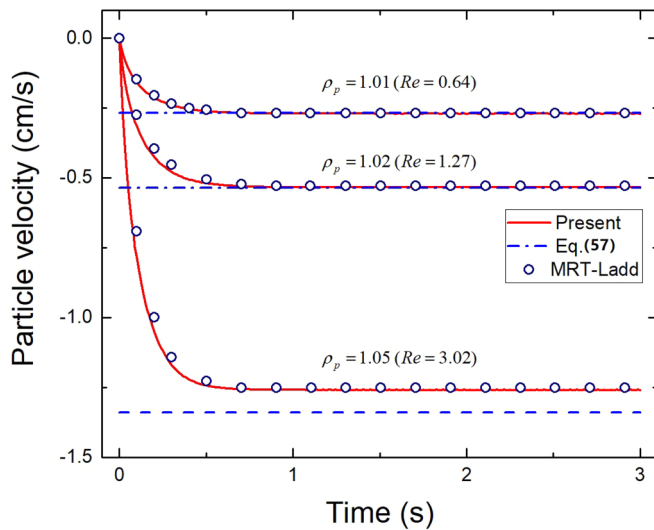


FIG. 4. Comparison of the vertical velocities of the particle during sedimentation for different particle densities. The number in the blanket of each case is the particle Reynolds number.

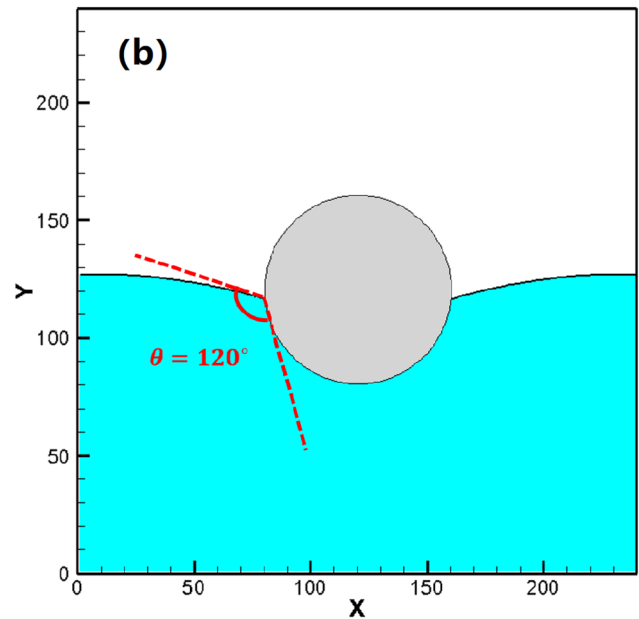
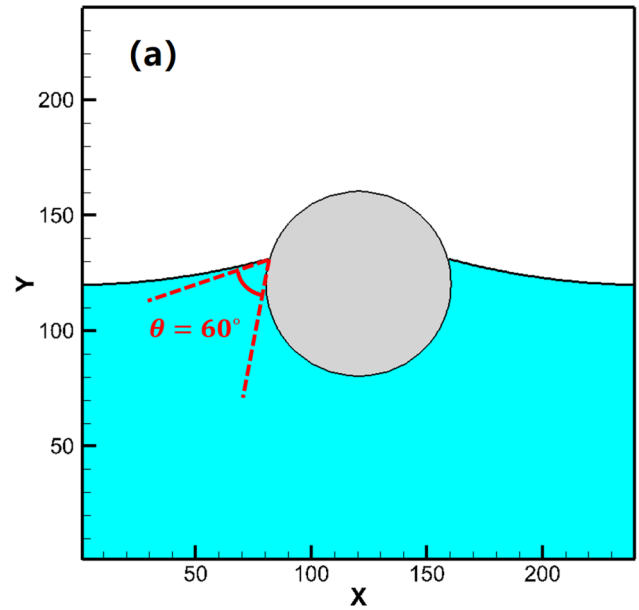


FIG. 5. The contact angles on a stationary cylinder under two different wetting conditions: (a) $\theta = 60^\circ$, (b) $\theta = 120^\circ$.

When a solid subject is floating in the fluid-fluid interface, the capillary force that acts on the subject arises due to the wettability. Another significant issue is how to obtain the capillary force. Connington [38] proposed a complicated algorithm; it needs to find the contact line on the surface of particle by the phase-field value, then compute the average surface tension force for each element by taking the integral of it. The large computation amount and less flexibility are its main drawbacks. However, in our model the capillary force arises spontaneously from the combination of the multiphase lattice Boltzmann model and momentum exchange method, which is also found in the simulation of the multiphase flow past a static circular cylinder [36]. We impose a specified contact angel at a solid boundary using the predictor-corrector

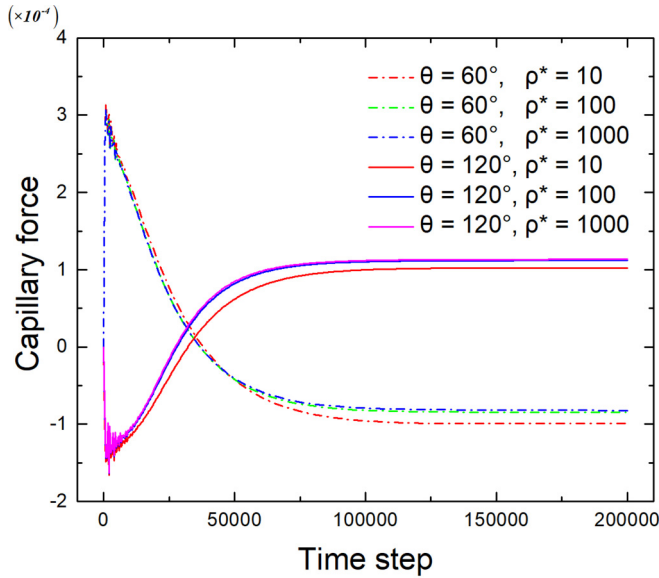


FIG. 6. Variations of the vertical capillary force of a stationary circular cylinder.

scheme based on free energy theory, where the three-phase contact line forms at the solid boundary, then we apply the bounce-back method, and the capillary force on the particle can be obtained by fluid-structure coupling interaction directly, which is in accordant with the physical mechanisms.

As shown in Fig. 6, the fluids exert a negative (downward) force on the cylinder with $\theta = 60^\circ$, while the net force experienced by the other cylinder with $\theta = 120^\circ$ is positive (upwards). Furthermore, the density and viscosity ratios have little influence on the capillary force and it is dominated by the surface tension σ and contact angle θ .

C. Sinking of a horizontal cylinder from an air-water interface

In order to check the test the performance of this method for liquid-gas-solid problem in the presence of a moving contact line, sinking of a circular cylinder from the water surface is now investigated, which has been studied experimentally by Vella *et al.* [39] and has also been investigated by Ding [40] through numerical simulation.

As show in Fig. 7, a circular cylinder lies horizontally at the interface between the water and air. The height h is the distance between the cylinder’s center and the undeformed free surface. The angle β is used to describe the position of contact line. In this simulation, the cylinder is placed in the liquid-gas interface and is half-immersed. A rectangle with the size of 1040×640 is chosen as the computational domain,

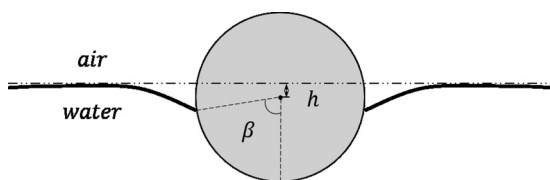


FIG. 7. Geometry of a cylinder lying horizontally at the interface between water and air.

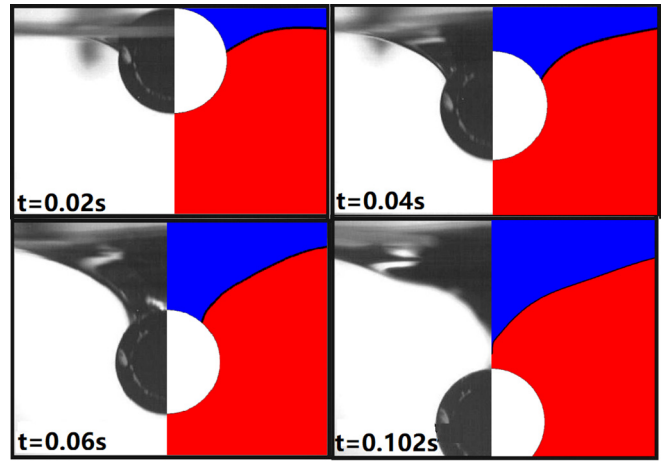


FIG. 8. Snapshots of sinking motion for a cylinder at different times. In each subfigure the experimental data [39] (left) are placed side by side with the numerical results (right).

which is sufficiently wide so that capillary waves reflected by solid wall will not affect the sinking dynamics of the cylinder, and the diameter of the cylinder is set as $D = 80$. The four boundaries are assumed to be the solid walls with a contact angle of 90° . The distance between the initialized horizontal interface and the bottom wall boundary is $5.6D$. We choose $(\sigma / \rho_H g^3)^{1/4}$ and $(\sigma / \rho_H g)^{1/2}$ as the characteristic time and length, respectively, according to the literature [39]. The density ratio ρ^* and viscosity ratio μ^* are set as 773 and 48 in accordance with water-air, the relaxation time τ_L and τ_H are set to be 0.05 and 0.0031. In this simulation, we choose the same dimensionless numbers as the experiments [39]: $Re = 250$, $We = 0.138$, $Bo = 3.478$. The wettability of the cylinder is represented by $\theta = 111^\circ$, which is the averaged value of the contact angles measured in the experiments [39].

Figure 8 shows the snapshots of the sinking dynamics of the cylinder, including the experimental results [39] and our numerical results. In this simulation, the cylinder’s weight plays the dominant role and it is larger than the hydrodynamic force and capillary force, thus the cylinder sinks into the water. In this process, the interface forms significant deformation and the contact line gradually moves to the peak of the cylinder and detaches from it ultimately. The position of the contact line relative to the cylinder can be represented by β , and the position of the cylinder relative to the initial water surface is denoted by $H = h/D$. Figures 9 and 10 quantitatively show β and H as a function of nondimensional time t , compared with the experimental data [39]. It has been found that the contact line slips past the cylinder at a relative low velocity at the beginning, then it comes to the later stage, in which the angular position of the contact line β increases approximately linearly in time and it agrees with the experimental data.

D. Self-assemblies of floating cylinders an air-water interface

A simulation study on the self-assemblies of several cylinders partially immersed in a fluid layer on the substrate is carried out. Capillary interactions provide a versatile route for structure formation. The particles at the liquid-gas interface can distort the interfaces to create an associated energy

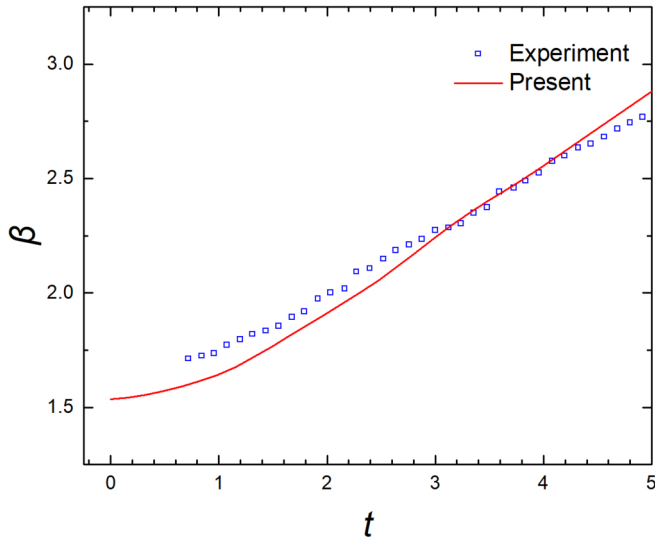


FIG. 9. The position of the contact line as a function of nondimensional time t .

field. When neighboring distortions overlap, particles interact to minimize interfacial area, creating forces that pull them into ordered structures [41,42]. Ding [40] has performed a simulation of three cylinders at the liquid-gas interface. In this work, a similar simulation is carried out to investigate the self-assembly process driven by the capillary tension.

Three identical cylinders A, B, C float at the air-water interface. The diameter of the cylinder is set as $D = 20$, the wettability is $\theta = 60^\circ$. A rectangle with the size of 160×160 is chosen as the computational domain, and the cylinders are initially half immersed in the fluid. The density ratio ρ^* and viscosity ratio μ^* is set as 773 and 48 in accordance with water-air, the relaxation time are $\tau_L = 0.1$ and $\tau_H = 0.0062$. The four boundaries are assumed to be the solid walls, with a contact angle of 90° . The distances between the right wall and

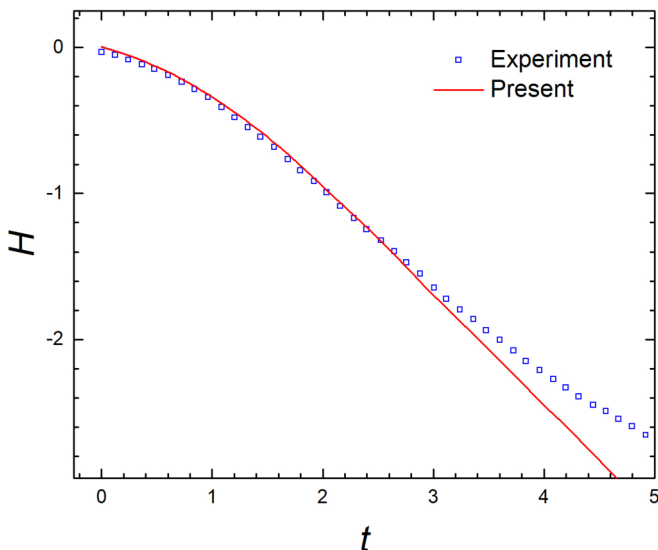


FIG. 10. The cylinder's center position as a function of nondimensional time t .

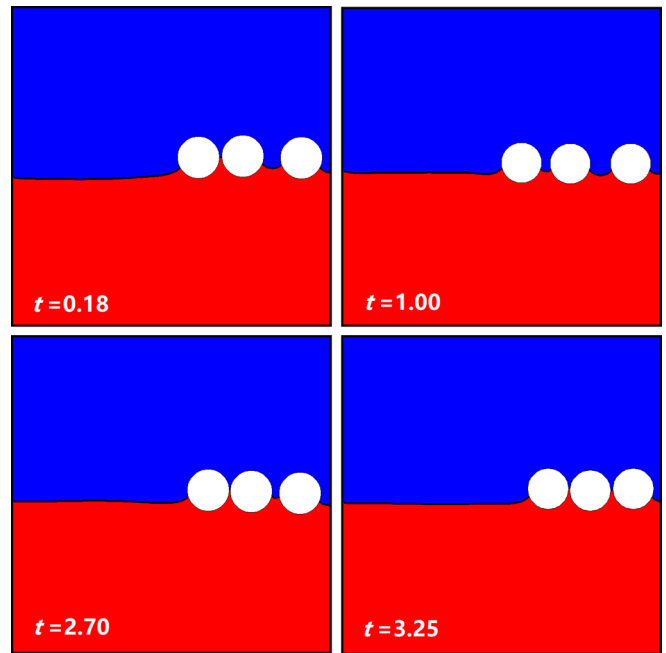


FIG. 11. Self-assembly movement of cylinders A, B , and C at different times $t = 0.18, t = 1.00, t = 2.70$, and $t = 3.25$.

the centers of A, B and C are $7, 4.5$, and $1.5 D$, respectively. In this simulation, we choose D as the characteristic length, and the inertial-capillary time $T = \sqrt{\rho_H D^3 / \sigma}$ as the characteristic time, and we consider a test case with dimensionless numbers as $Re = 40, We = 0.16, Bo = 4.0$.

Figure 11 shows snapshots of the self-assembly of three cylinders. To describe the details of the process, we characterize the horizontal and vertical positions of the three cylinders in Figs. 12 and 13. It can be seen that the evolution of the distance of centers between three cylinders falls into three stages. In the first stage ($t < 1.2$), cylinder C is nearly stationary, but both the cylinder A and cylinder B move towards the right, but

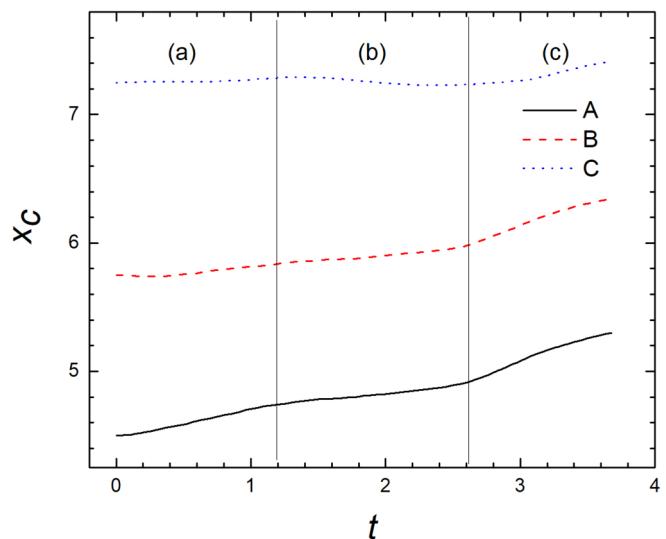


FIG. 12. The horizontal position of the cylinders vs time.

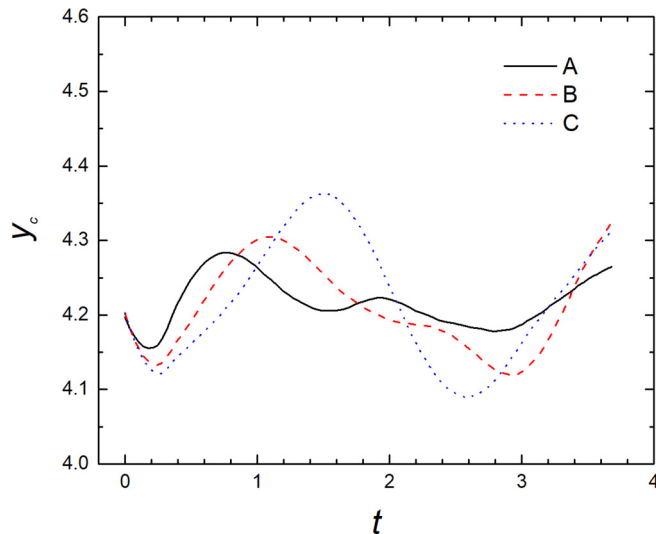


FIG. 13. The vertical position of the cylinders vs time.

the velocity of cylinder *A* is obviously larger than cylinder *B*, in other words, the cylinder *A* approaches cylinder *B* quickly in this stage. In the second stage ($1.2t < 2.6$), the cylinders *A* and cylinders *B* came into contact and move toward the right as a unit until they run into the cylinder *C*. In the third stage ($2.6 \leq t$), the three cylinders form a unit and moves toward the right wall. The horizontal movement of the three cylinders is also accompanied by their vertical oscillation on the water surface, which is consistent with the results in the literature [40].

IV. CONCLUSION

In the present work, we develop a method to simulate LGS flow. Our algorithm combined a phase-field-based model to handle the multiphase flow with a high density ratio as well as the particle transport. In order to make the algorithm more stable, we combine the implicit particle velocity update scheme and the modified ME method. The curved boundary treatment with second-order accuracy based on velocity interpolation is proposed. We also developed a numerical technique to implement wetting boundary conditions on curved surfaces without approximating the curved boundary as a staircase.

To validate the incorporation of this new algorithm, we first demonstrate that the method is accurate when solid objects are contained inside bulk fluid regions of the flow, then we simulated the contact line motion on a single circular cylinder fixed in the interface. It was found that the surface tension force associated with the interface acting on the solid structures can be captured by the ME method in this model. Moreover, the suitability of this method is tested by performing studies of sinking dynamics of a circular cylinder from the water surface due to gravity and the self-assembly process of multiple floating cylinders on the water surface.

ACKNOWLEDGMENTS

This work is supported by National Key R&D Program of China (Grant No. 2018YFB2000800) and the National Natural Science Foundation of China (Grants No. 51735006 and No. 11802159).

- [1] E. Tekin, P. J. Smith, and U. S. Schubert, *Soft Matter*, **4**, 703 (2008).
- [2] E. Dickinson, *Curr. Opin. Colloid Interface Sci.* **15**, 40 (2010).
- [3] T. N. Hunter, R. J. Pugh, G. V. Franks, and G. J. Jameson, *Adv. Colloid Interface Sci.* **137**, 57, (2008).
- [4] W. L. Li and W. Q. Zhong, *Powder Technol.* **286**, 766 (2015).
- [5] X. S. Sun and M. Sakai, *Chem. Eng. Sci.* **134**, 531 (2015).
- [6] Y. G. Xu, M. Y. Liu, and C. Tang, *Chem. Eng. J.* **222**, 292 (2013).
- [7] A. J. C. Ladd, *J. Fluid Mech.* **271**, 285 (1994).
- [8] A. J. C. Ladd, *J. Fluid Mech.* **271**, 311 (1994).
- [9] X. Y. He, S. Y. Chen, and R. Y. Zhang, *J. Comput. Phys.* **152**, 642 (1999).
- [10] A. K. Gunstensen, D. H. Rothman, S. Zaleski, and G. Zanetti, *Phys. Rev. A* **43**, 4320 (1991).
- [11] M. R. Swift, E. Orlandini, W. R. Osborn, and J. M. Yeomans, *Phys. Rev. E* **54**, 5041 (1996).
- [12] X. W. Shan and H. D. Chen, *Phys. Rev. E* **47**, 1815 (1993).
- [13] K. Stratford, R. Adhikari, I. Pagonabarraga, and J. C. Desplat, *J. Stat. Phys.* **121**, 163 (2005).
- [14] K. Stratford, R. Adhikari, I. Pagonabarraga, J. C. Desplat, and M. E. Cates, *Science* **309**, 2198 (2005).
- [15] P. Stansell, K. Stratford, J. C. Desplat, R. Adhikari, and M. E. Cates, *Phys. Rev. Lett.* **96**085701 (2006).
- [16] A. S. Joshi and Y. Sun, *Phys. Rev. E* **82**, 041401 (2010).
- [17] A. S. Joshi and Y. Sun, *Phys. Rev. E* **79**, 066703 (2009).
- [18] F. Gunther, F. Janoscsek, S. Frijters, and J. Harting, *Comput. Fluids* **80**, 184 (2013).
- [19] E. M. Herzig, K. A. White, A. B. Schofield, W. C. K. Poon, and P. S. Clegg, *Nat. Mater.* **6**, 966 (2007).
- [20] K. W. Connington, M. Z. Miskin, T. Lee, H. M. Jaeger, and J. F. Morris, *Int. J. Multiphase Flow* **76**, 32 (2015).
- [21] J. Onishi, A. Kawasaki, Y. Chen, and H. Ohashi, *Comput. Math. Appl.* **55**, 1541 (2008).
- [22] F. Jansen and J. Harting, *Phys. Rev. E* **83**, 046707 (2011).
- [23] G. B. Davies, T. Krüger, P. V. Coveney, and J. Harting, *J. Chem. Phys.* **141**, 154902 (2014).
- [24] Y. Chen, Q. J. Kang, Q. D. Cai, M. R. Wang, and D. X. Zhang, *Commun. Comput. Phys.* **18**, 757 (2015).
- [25] G. Y. Liang, Z. Zeng, Y. Chen, J. Onishi, H. Ohashi, and S. Y. Chen, *J. Comput. Phys.* **248**, 323 (2013).
- [26] A. Fakhari, T. Mitchell, C. Leonardi, and D. Bolster, *Phys. Rev. E* **96**,053301 (2017).
- [27] P. H. Chiu and Y. T. Lin, *J. Comput. Phys.* **230**, 185 (2011).
- [28] Y. Q. Zu and S. He, *Phys. Rev. E* **87**, 043301 (2013).
- [29] P. Lallemand and L. S. Luo, *Phys. Rev. E* **61**, 6546 (2000).
- [30] Z. L. Guo, C. G. Zheng, and B. C. Shi, *Phys. Rev. E* **65**, 046308 (2002).
- [31] B. Wen, C. Zhang, Y. Tu, C. Wang, and H. Fang, *J. Comput. Phys.* **266**, 161 (2014).

- [32] N.-Q. Nguyen and A. J. C. Ladd, *Phys. Rev. E* **66**, 046708 (2002).
- [33] T. Zhang, B. C. Shi, Z. L. Guo, Z. H. Chai, and J. H. Lu, *Phys. Rev. E* **85**, 016701 (2012).
- [34] T. Lee and C. L. Lin, *J. Comput. Phys.* **206**, 16 (2005).
- [35] Y. Xie, O. Wodo, and B. Ganapathysubramanian, in *Advances in Computational Fluid-Structure Interaction and Flow Simulation*, edited by Y. Bazilevs and K. Takizawa, Modeling and Simulation in Science, Engineering and Technology (Birkhäuser, Cham, 2016), pp. 203–215.
- [36] A. Fakhari and D. Bolster, *J. Comput. Phys.* **334**, 620 (2017).
- [37] L. Wang, Z. L. Guo, B. C. Shi, and C. G. Zheng, *Commun. Comput. Phys.* **13**, 1151 (2013).
- [38] K. W. Connington, T. Lee, and J. F. Morris, *J. Comput. Phys.* **283**, 453 (2015).
- [39] D. Vella, D. G. Lee, and H. Y. Kim, *Langmuir* **22**, 2972 (2006).
- [40] H. R. Liu, P. Gao, and H. Ding, *J. Comput. Phys.* **348**, 45 (2017).
- [41] I. B. Liu, N. Sharifi-Mood, and K. J. Stebe, *Annu. Rev. Condens. Matter Phys.* **9**, 283 (2018).
- [42] G. M. Whitesides and B. Grzybowski, *Science* **295**, 2418 (2002).